Standard Penetration Testing in a virtual calibration chamber

Zhang, Ningning; Arroyo, Marcos; Ciantia, Matteo; Gens, Antonio; Butlanska, Joanna

Published in:
Computers and Geotechnics

DOI:
10.1016/j.compgeo.2019.03.021

Publication date:
2019

Standard Penetration Testing in a virtual calibration chamber

Ningning Zhang[a,*]; Marcos Arroyo[a]; Matteo Oryem Ciantia[b]; Antonio Gens[a]; Joanna Butlanska[a]

[a] *Department of Geotechnical Engineering and Geosciences, Technical University of Catalonia (UPC), SPAIN*

[b] *School of Science and Engineering, University of Dundee, UK*

*Corresponding author at: Department of Geotechnical Engineering and Geosciences, Technical University of Catalonia (UPC), SPAIN. E-mail address: ningning.zhang@upc.edu (N. Zhang)

ABSTRACT

The virtual calibration chamber technique, based on the discrete element method, is here applied to study the standard penetration test (SPT). A macro-element approach is used to represent a rod driven with an impact like those applied to perform SPT. The rod is driven into a chamber filled with a scaled discrete analogue of a quartz sand. The contact properties of the discrete analogue are calibrated simulating two low-pressure triaxial tests. The rod is driven changing input energy and controlling initial density and confinement stress. Energy-based blowcount normalization is shown to be effective. Results obtained are in good quantitative agreement with well-accepted experimentally-based relations between blowcount, density and overburden. It is also shown that the tip resistance measured under impact dynamic penetration conditions is close to that under constant velocity conditions, hence supporting recent proposals to relate CPT and SPT results.

KEYWORDS: Discrete element method; Standard penetration test; Blowcount; Energy; Fontainebleau sand

List of notations

σ_{max} peak compressive stress in impact waves

μ friction coefficient

$\Delta\rho$ penetration depth per blow

ρ_r mass density of rod material

v Poisson's ratio

η_d impact or dynamic efficiency ratio

I, II, III, IV and V phases in dynamic process

a cross-sectional area of rod

A_h cross-sectional area of hammer

B and C material dependent parameters

c wave propagation velocity in rod

d_1 and d_2 diameters of the two spheres in contact

d_c rod outside diameter

D coefficient

D_c chamber diameter

D_r relative density

D_{50} mean grain size

e_{max} maximum void ratio

e_{min} minimum void ratio

E elastic modulus of rod material

E_{blow} energy delivered by hammer to driven rod

ER ratio of energy delivered by hammer to theoretical driving energy

F_{max} maximum impact force

F_n impact force for nth (n >1) compression pulse

$|F_n|$ magnitude of normal contact force

$F_{P\_j}^t$ vertical reaction from particle j at rod tip at time t

$F_{s\_i}^t$ vertical reaction force from particle i along shaft at time t

F_{tot}^t total force acting on rod at time t

F_{drv}^t imposed driving force at time t

g	gravitational acceleration
G	shear modulus
G_r	gravitational force of rod
h	falling height of hammer
H	chamber height
k_n	normal contact stiffness
k_s	shear contact stiffness
l	length of rod
L	length of hammer
m_h	hammer mass
m_r	rod mass
n_p	rod/particle ratio
N	SPT blow counts
N_{60}	dynamic resistance normalized by 60% energy efficiency
P_0	confining pressure
q_d	dynamic tip resistance
q_e	static tip resistance
r	hammer-rod impedance ratio
R_d	chamber/rod ratio
Δt	timestep
t	time duration of each compression wave
t_{max}	maximum impact time
$t_{\_eq}$	equilibration time
t_1, t_2, t_3 and t_4	characteristic time points identified in penetration curve
U	sphere overlap
U_R	rod potential work
v_{peak}	rod peak velocity
$v_r(t)$	driven rod velocity history
V_h	velocity of hammer at impact
W_H	hammer input work
$\dot{x}^{t+\Delta t}$	velocity component of rod

$\dot{z}^{t}$ vertical velocity of rod at time t

$\dot{z}^{t+\Delta t}$ vertical velocity of rod at time ($t+\Delta t$)

1. INTRODUCTION

Dynamic probing involves driving a device into the soil by striking it with a hammer. This technique is employed in several site investigation tests such as the Standard Penetration Test (SPT), Becker Penetration Test (BPT), Dynamic Cone Penetration Test (DCPT) or light dynamic penetrometers (e.g. Panda; [1]). Of these, the Standard Penetration Test (SPT) remains as one of the most popular in-situ testing procedures [2], frequently used to estimate soil properties [62, 18], foundation design parameters and evaluate liquefaction potential [49].

Tests based on dynamic probing have several advantages: they are widely available, economical and robust. They can be used in any ground condition, particularly on coarse materials such as gravels, ballast or weathered rock, where most alternatives fail. Dynamic probing tests also have important limitations. First: they are difficult to control precisely, which is detrimental for test repeatability. Second: they usually produce a single measurement per test (for instance *N*, number of blows to drive a sampler 300 mm in the ground) and such a restricted output inherently limits interpretation. Third: the mechanics of their interaction with the ground are poorly understood, which forces interpretation by strictly empirical approaches. All these shortcomings have been addressed in previous research, but to a different extent.

Many efforts have concentrated in improving test control and repeatability. A major step in this direction was made when energy input measurements were developed for the SPT [3, 4]. Recording the energy input from hammer blows on the rod-sampler system allowed to introduce an energy normalized blow number, N_{60}, which was shown to improve significantly test output repeatability [5, 6]. The energy-normalized value N_{60} is now a required basis for quantitative SPT interpretation [7, 8]. Further research [9, 10, 11] has progressively refined the methodology applied to measure and extract the amount of energy actually delivered to the driven sampler. Energy input measurement techniques have been also developed for other dynamic probes, like the Panda or the BPT [12].

Several proposals are also available to increase the number of results obtained from each test. Some, like the torsional SPT or SPT-T [13], require extra specific procedural steps. Perhaps more interesting are those that obtain extra results from the same procedure, for instance through interpretations of SPT based on penetration per blow, $\Delta\rho$, [2] or enhanced dynamic data acquisition for light dynamic penetrometers [14].

Testing under well controlled conditions is essential to understand the factors underlying the dynamic interaction between probes and soils. In the laboratory in situ tests are typically studied using calibration chambers. Because of the complexities involved, comparatively little calibration chamber work on dynamic driven probes has been reported [15, 16, 17]. Experimental data supporting dynamic test interpretation is then mostly gathered from field studies, [6, 18]. Unfortunately, field studies are costly, slow and subject to numerous uncertainties.

In principle, numerical simulation may be also used to perform controlled dynamic probing experiments. This, however, is difficult to put into practice, since dynamic probing involves large displacements, large strains, moving boundaries and high loading frequencies. It is not clear which numerical technology will be more appropriate for this kind of study. For granular soils, models based on the Discrete Element Method (DEM) [19] appear attractive because 1) they are able to deal with large displacement contact problems in a dynamic setting, 2) they have relatively few free material parameters to calibrate, and 3) they can easily incorporate grain scale properties such as crushability, which are known to strongly affect the results of dynamic probing tests [20].

The use of 3D DEM models to create virtual calibration chambers (VCC) is well established for quasi-static tests like the cone penetration test (CPT) [21, 22, 23, 24] or the Marchetti dilatometer [25]. VCC for light dynamic penetrometers have been used by Breul and co-workers, mostly using 2D models [26, 27] but sometimes also in 3D [28]. A similar approach has been also recently used to study the impact of torpedo anchors [29].

The objective of this work is to demonstrate the potential of the DEM virtual calibration chamber technique to study standard penetration testing in granular soils. In previous VCC studies [21, 23, 25] a specific physical test series has been selected for comparison. For the case of SPT such approach was not possible because the old key studies [15, 16] lacked energy measurements while more contemporary research [17] was too succinctly described. Furthermore, directly mimicking these studies would have required simulation of a borehole excavation phase, which introduces distracting complications. It was then decided to validate the VCC method in this case by examining if the results obtained for a more generic case would fit into well-established general empirical trends.

In the following sections we describe how a 3D VCC model was built, filled with a calibrated discrete analogue of a representative quartz sand and then subject to a series of dynamic probes at varying confinement and density. The results obtained are then quantitatively compared with the existing physical database. The methodology employed to build the model is described in detail, paying particular attention to those aspects involved in the specification of the dynamic driving force. For reasons of space, the work presented here will focus on macro-scale results, leaving aside for the moment the possibilities of DEM models to explore the microscale [30].

2. MODEL DESCRIPTION

2.1 A DISCRETE ANALOGUE OF FONTAINEBLEAU SAND

Fontainebleau sand is a standard test silica sand that has been extensively used in geotechnical research [31, 32, 33]. Some of its physical properties are presented in Table 1.

A discrete analogue of Fontainebleau sand is obtained using the DEM code PFC3D [34], which is employed in all the simulations described in this work. Particle crushing effects (e.g. [40]) are not included here, and the discrete elements employed are always unbreakable spheres. To roughly mimic the effect of non-spherical particle shapes, particle rotation was inhibited, directly fixing the rotational degrees of freedom of the particles. This simplified approach, can be traced back to Ting et al. [35] and was successfully applied in previous work with granular materials [21, 36, 37, 38, 39]. More refined consideration of particle shape effects may be obtained using rolling-resistance contact models (e.g. [41, 61]). However, such refinements complicate calibration and were thus left aside in this first exploratory study.

The constitutive contact law describing force-displacement interaction between particles is elasto-plastic. A friction coefficient μ defines the slip behavior at contacts. Contact rigidity is given by the ratio of contact forces and incremental displacements in the normal and tangential directions. In this study, the simplified Hertz-Mindlin theory is used to define the normal and tangential rigidity at each contact:

$$k_n = \left(\frac{2\langle G \rangle \sqrt{2\frac{d_1 d_2}{d_1 + d_2}}}{3\left(1 - \langle v \rangle\right)} \right) \sqrt{U} \qquad (1)$$

$$k_s = \left(\frac{2\left(\langle G \rangle^2 3\left(1 - \langle v \rangle\right) \frac{d_1 d_2}{d_1 + d_2} \right)^{1/3}}{2 - \langle v \rangle} \right) \left| F_n \right|^{1/3} \qquad (2)$$

Where, U is the sphere overlap, $\left|F_n\right|$ is the magnitude of the normal contact force and the $\langle\ \rangle$ brackets indicate the mean value of the quantity considered of the contacting elements; G is the shear modulus, v is the Poisson's ratio and d_1, d_2 are the diameters of the contacting elements.

The contact model properties (G, μ, v) (Table 2) were taken from a previous calibration made by Ciantia et al. [42]. Since a new version of the PFC software was employed here, the calibration set of triaxial compression tests was simulated again. The numerical model response was thus compared anew with the macroscopic responses of Fontainebleau sand in two low-pressure (100 kPa) triaxial compression tests reported by Seif El Dine et al. [32]. The numerical tests were performed using a cubical cell of 4 mm in size containing 11,000 elements. Element sizes for this cubical cell were selected to closely match the PSD of Fontainebleau NE34 sand (Figure 1). The matching obtained (Figure 2) is considered adequate, given the simplicity of the model.

2.2 CHAMBER CONSTRUCTION

The construction of 3-dimensional VCC models followed a procedure described previously [21, 23]. A calibration chamber with 0.5 m height and 0.76 m diameter was built using wall elements. Discrete elements filling up the chamber have the same contact properties and shape as those used for calibration. However, to obtain a model with a manageable number of particles, their size was uniformly upscaled applying a uniform scaling factor of 79, leading to a rod/particle ratio, n_p = 3.06, similar to that employed in previous studies [21, 23]. The resulting size distribution is a shifted version of that from the original sand (Figure 1). All the chamber boundaries were set to be frictionless.

Geometrical model details can be seen in Figure 3 and Table 3. The choice of chamber dimensions was inspired by previous experimental work on the topic (see Table 4). In most of those studies, SPT was performed at various locations within the chamber plan, apparently without major impact on the test results. Here only testing at the axis of the chamber has been attempted. The resulting chamber/rod diameter ratio is 15, a ratio that results in some chamber size effects for fully penetrating CPT (e.g. [30]). It is not clear that such effects are equally relevant for the short dynamic probes performed here.

Tests were performed with the material in the chamber at pre-established values of density and isotropic confinement. The radius expansion method (REM) was used to fill the chamber. To attain the target porosity, inter-particle friction was reduced while all chamber walls were servo controlled to maintain an isotropic compression of 5 kPa. After equilibration, inter-particle friction was reset to the calibrated value and isotropic stress was ramped up to the target level. In all simulations a local damping of 0.05 [43] was employed and no viscous damping was considered. Detailed energy balances of the VCC during driving

[44] show that such a small amount of damping results in negligible dissipation compared with that due to contact friction.

A flat-ended rod of outside diameter 50.8 mm was created by using frictional rigid walls. Rod diameter has been selected to coincide with the normalized dimension of the SPT sampling tube. A closed ended rod is a feature of some dynamic probing tests, like the BPT, and may be also interpreted as representing a plugged SPT sampler. Sampler plugging in sand has been assumed in previous SPT interpretation methods [2]. Realistic modelling of the plugging phenomenon is beyond the scope of this work as would likely require applying a significantly smaller particle scaling factors. The contact model between rod and particles is also a simplified Hertz-Mindlin with limiting friction. The parameters for the rod are given in Table 2. The entire rod surface is assumed frictional.

During rod penetration, the VCC radial boundary was maintained at constant radial stress using a servo-mechanism. The same stress level was also maintained at the top horizontal boundary. On the other hand, the bottom horizontal boundary was fixed and no displacement was allowed.

When performing a SPT the first 15 cm of penetration are described as a seating drive, and not considered when evaluating the test result. A similar procedure was employed here and the rod was firstly pushed into the sample at a constant rate of 40 cm/s until the tip reached a depth of 15 cm. This also had the advantage of minimizing any major influence of the top boundary during driving [30]. On the other hand, simply stopping static penetration will result in locked-in residual forces against the rod. Therefore, after the 15 cm static penetration phase, a servo control was applied to slightly pull back the rod from the sample, restoring the vertical total force on the rod to zero (see example in Figure 4). At this point, the model was deemed to be in an appropriate state for launching dynamic penetration.

2.3 DYNAMIC DRIVING

2.3.1 REPRESENTATION OF DRIVEN RODS

Different approaches have been used to mimic driven rods in DEM simulations. Escobar et al. [26], using 2D DEM, represented a solid steel rod using bonded particles. This allows to model elastic wave propagation through the rod. On the other hand, and because of the large contact rigidity necessary to model steel, the time step required by the explicit time integration method becomes very small, and large computational costs are incurred.

A computationally less costly alternative [28] is to represent the rod using a macro-element. This was done here by bundling walls together and imposing on them a uniform rigid-body motion that approximates that of the rod. The wall-bundle is forced to move vertically and, to ensure a dynamically correct motion, the following equation is used:

$$\dot{Z}^{t+\Delta t} = \dot{Z}^{t} + \frac{F_{tot}^{t}}{m_r}\Delta t \qquad (3)$$

Where, $\dot{Z}^{t+\Delta t}$ and $\dot{Z}^{t}$ are the vertical velocities of rod at time (t+Δt) and t, respectively, Δt is the time step and m_r is an assigned rod mass (see below). F_{tot}^{t} is the total force acting on the rod, i.e.

$$F_{tot}^{t} = \sum_i F_{s\_i}^{t} + \sum_j F_{p\_j}^{t} + F_{drv}^{t} + m_r g \qquad (4)$$

Where, $F^t_{s\_i}$ is the vertical reaction force from particle *i* along the shaft, $F^t_{p\_j}$ is the vertical reaction from particle *j* at the rod tip, F^t_{drv} is an imposed driving force and *g* is the gravitational acceleration.

The virtual rod mass, m_r is determined from values of rod length *l* and rod material density ρ_r that are assigned in the specification of the imposed driving force.

2.3.2 SPECIFICATION OF DRIVING FORCE

In Eq (4), a time-dependent force input is specified to represent the driving force. The force input employed in this work was intended to approximate the characteristics of an SPT blow.

Recent experimental work [45, 46] indicates that a single SPT blow may result in relatively complex time-force signals in the rod, with several impacts due to hammer rebound and/or hammer delay and subsequent catch-up. The characteristics of the input force are thus strongly dependent on the particularities of the driving mechanism and the soil nature. Structural dynamic 1D models may be used to predict input force characteristics for a particular configuration of the impact mechanism [3, 10]. Such approaches seemed unnecessarily complex for the exploratory work presented here. Instead, a relatively simple but realistic input force was derived from a simplified hammer-rod interaction analysis. Fairhurst [47] proposed an elastodynamic model to describe the time history of an ideal impact force between a hammer and a rod. It assumes cylindrical pieces, no separation between hammer and rod and takes into account the transmission, at the hammer/rod interface, of rebound waves from the upper hammer end as successive compression pulses of progressively reduced stress levels.

According to this model the peak compressive wave stress during the first impact, σ_{max}, is given by

$$\sigma_{\max} = \rho_r c \left(\frac{V_h}{1+r} \right) \qquad (5)$$

Where, *c* is the wave propagation velocity in the rod, V_h is the hammer impact velocity, and *r* is the hammer-rod impedance ratio, equal to the ratio of cross-sectional area of the rod, *a*, to the area of the hammer A_h, if both are of the same material. The wave propagation velocity is calculated as

$$c = \sqrt{E / \rho_r} \qquad (6)$$

Where, *E* is the elastic modulus of the rod material. The hammer impact velocity is here calculated through

$$V_h = \eta_d \sqrt{2gh} \qquad (7)$$

Where, *h* is the falling height of hammer and η_d represents a dynamic efficiency ratio. Unless otherwise stated, in all the simulations below, the value of this parameter is always set as 1. From the relations above it follows that the maximum impact force can be expressed as

$$F_{\max} = \frac{\eta_d a \sqrt{2ghE\rho_r}}{1+\left(\frac{a}{A_h} \right)} \qquad (8)$$

The corresponding impact force F_n for the nth (n >1) compression pulse, is

$$F_n = F_{\max}\left(\frac{1-r}{1+r}\right)^{n-1} \quad \text{for } \frac{2(n-1)L}{c} < t < \frac{2nL}{c} \qquad (9)$$

Where, L is the hammer length and t defines the time duration of each compression wave.

The simulated impact is terminated at time $t_{max} = 2l/c$ after the start of impact, where l is the length of rod. This would be the time when an elastic wave reflected from the rod tip as a tension wave returns to the rod head and pulls it away from the hammer. The maximum number of completed stress steps n before loss of hammer contact is then given by the integer part of l/L. In experimental records of SPT blows, [3, 46], this round-trip time t_{max} coincides, approximately, with the duration of the first hammer impact which is that delivering the largest amount of energy to the sample.

The parameters describing the simulated driving system are collected in Table 5. The hammer and the rod are assumed to be of the same steel material. The rod is assumed to be 10 m long. The hammer diameter is assumed to be twice that of the rod and its length (approximately 1/10 of that if the rod) was computed from its assumed mass and steel density. Using these inputs, a 63.5 kg hammer falling from a height of 0.76 m will generate a 4 ms impact force with F_{max}= 251 kN (Figure 5).

2.3.3 BLOWCOUNT, BLOW ENERGY AND ENERGY RATIO

The value of equivalent blow counts N is determined by the ratio of the reference 30 cm distance by the penetration depth per blow $\Delta\rho$. Following a similar reasoning to that presented by Odebrecht et al. [11] the energy delivered by the driven rod to the VCC in a given blow, E_{blow}, is computed as the sum of hammer input work W_H and work done by the rod self-weight, U_R. These energy terms can be calculated by integrating the work done by the impact force and gravitational forces on the driven rod,

$$E_{blow} = W_H + U_R = \int_0^{t\_eq} F_{drv}(t)v_r(t)dt + m_r g\int_0^{t\_eq} v_r(t)dt \qquad (10)$$

Where, $v_r(t)$ represents the driven rod velocity history, which is an output of the test and the upper limit of the integral, $t_{\_eq}$ is the time for equilibration.

Following standard practice, an energy ratio is then computed normalizing the energy delivered by the theoretical driving energy of an SPT (given by a hammer mass, m_h = 63.5 kg; fall height h = 0.76 m)

$$ER = \frac{E_{blow}}{m_h g h} \qquad (11)$$

Depending on various hammer types and testing details, the energy ratio in practical field testing can vary in a wide range from 30% to 90% [5, 6, 11, 48]. It has become common practice to normalize the blow count, taking into account the energy ratio delivered to obtain a standardized blow number N_{60} (corresponding to blows of 60% energy efficiency) as:

$$N_{60} = \frac{ER}{60}N \qquad (12)$$

2.4 SIMULATION PROGRAM

The main soil state variables affecting dynamic penetration results are density and stress level. These are represented here by relative density D_r and mean confining pressure P_0. The specimens were generated by combining four density levels, namely very dense (D_r=*82%*), dense (D_r=*72%*), medium (D_r=*60.5%*) and loose (D_r=*38.6%*) and three confining stress levels (P_0 =100 kPa, 200 kPa and 400 kPa). A series of impact tests were conducted in all the 12 specimens by prescribing the same force-time signal proposed previously. The main characteristics of these DEM-based tests are collected in Table 6.

3. RESULTS

Even restricting ourselves to the macroscopic level, a wealth of results are available, since tip resistance, hammer input energy, rod motion features are continuously tracked in time. Before examining the effects of the main controlling variables on test results it is interesting to consider in detail the dynamics of a single blow.

3.1 IMPACT DYNAMICS

The evolution in time of rod velocity, rod acceleration, rod tip position (i.e. penetration depth) and tip resistance is illustrated in Figure 6 for a representative example (test Loose_200 in Table 6). The record was interrupted after 0.15 s, as most variables had by then reached a stationary value.

A dynamic penetration curve (Figure 7) can be deduced from the previous results by representing tip resistance vs dynamic penetration (i.e. rod penetration minus the 0.15 m achieved statically). The dynamic penetration curves obtained appear very similar to those registered using instrumented dynamic penetrometers [14, 26]. Several characteristic points are identified in the penetration curve, corresponding to times t_1, t_2, t_3 and t_4. Using these characteristic times 5 phases (I, II, III, IV and V) are distinguished in the dynamic process (Figure 6).

The first phase (*I;* which might be called *"acceleration"*) corresponds to the period in which rod acceleration is negative (i.e. downwards), with t_1 selected as the time in which acceleration first changes sign (Figure 6b). Until this moment the imposed driving force is overcoming the soil resistance acting on the rod. Rod velocity attains then its maximum at 1.4 m/s, a value close to the anvil velocities under SPT registered by Lee et al. [46]. Phase *I* is also characterized by a quasi-linear rise in tip resistance. Shortly after t_1 the tip resistance begins to oscillate while penetration advances.

The second phase (*II; "deceleration"*) finishes when the velocity of the rod crosses zero at t_2. Of course, at this point penetration advance stops. In this phase soil resistance decelerates the rod with a relatively constant magnitude, hence reducing rod velocity at an almost constant rate. Penetration continues accompanied of large tip resistance oscillations -the largest of which is coincident with the only significant step in acceleration magnitude during this phase.

The third phase (*III; "unloading"*) corresponds to a period in which the rod rebounds and the tip is progressively unloaded until it becomes practically 0 at t_3. There is still some inertia in the system that is revealed in rod oscillations during phase *IV,* which lasts until the rod attains is final penetration depth at t_4.

The rod was driven to a permanent penetration of 0.026 m, corresponding to a blow number N = 12. Beyond that time, in phase *V*, only small oscillations in the residual tip resistance are visible, perhaps best seen as an indication of a somewhat insufficiently damped system.

3.2 PENETRATION AND DRIVING ENERGY

As recorded in Table 7 the energy ratios delivered to the chamber lie mostly within the 40% - 50% range. Those values are within the range of observed field energy ratios 30%-90% [49] although clustered towards the lower end. Note that, in the field, the energy delivered by a hammer blow frequently requires more time than the strict two-way rod wave trip time assumed here to establish $t_{max.}$ Figure 8 plots the energy ratio levels and the penetration per blow observed for all the different tested conditions of density and confining stress. A proportionality between these two magnitudes is evident from the figure, much like that observed by Schnaid et al [50] in field testing.

The energy normalization of blowcount in equation (12) implies that the normalized value is independent of the driving system characteristics or, equivalently, that N_{60} is only affected by soil properties (parameters and state). As noted before that was verified empirically by field testing, driving SPT at the same site with different, independently measured, energies [3, 6]. It seemed reasonable to check if this energy normalization is also verified in the VCC. To this end, a separate series of simulations was run, modifying the driving force history by the simple expedient of using different values of the dynamic efficiency ratio, η_d (0.7, 0.9, 1.0 and 1.2). All the other settings were maintained constant and therefore the driving time was kept constant at 4 ms. The different resulting force-time curves are illustrated in Figure 9.

The blows at different energy were simulated on specimen Dense_100. The results are summarized in Table 8 and both measured blowcounts, *N*, and normalized blowcounts N_{60} are presented in Figure 10. It is evident that the energy normalization works well, with all the normalized N_{60} values very close to one another.

3.3 INFLUENCE OF GROUND CONDITIONS ON PENETRATION RESISTANCE

There are a great number of soil-related factors known to influence the resistance to dynamic penetration, including void ratio, current stress levels, average particle size, coefficient of uniformity, particle angularity, cementation, aging, etc. For granular soils, however, a main focus has been always on establishing the relation between SPT blow count and relative density.

It was early noticed that, although the influence of relative density on SPT was very strong, it could not be considered separately from that of stress level. In a classical study, Gibbs and Holtz [15] used calibration chamber testing to explore the relation between *N*, relative density (D_r) and overburden pressure (P_0). Their results for dry sands were summarized by Meyerhof [51] in the following relation

$$N = 1.7 \times \left(\frac{D_r}{100} \right)^2 (0.145 P_0 + 10) \qquad (13)$$

where the overburden pressure P_0 is expressed in kPa.

Later calibration chamber studies (Table 4) of SPT in sands have proposed slightly different formulations, generally indicating a feebler effect of relative density than that observed by Gibbs and Holtz [15]. Differences are attributed [16, 17] to the effects of saturation, to details of the dynamic testing procedure or to fabric effects derived from specimen formation procedures (e.g. dynamic compaction vs pluviation). It is also clear that creating homogeneous tank-sized specimens of sand is a very difficult task, as shown by the large variability in results reported by Marcuson and Bieganouski [16].

Figure 11 compares the prediction of the summary equations proposed by different authors with the results obtained from the DEM simulations for the case in which P_0 equals 200 kPa. The DEM results appear to match very well the Meyerhof [51] expression. A more complete comparison with this classical experimental result is presented in Figure 12. It appears that the comparison deteriorates as the blow number increases, with the DEM simulation resulting in smaller blow-counts than those predicted by Meyerhof [51]. Because the blow energy applied by Gibbs and Holtz [15] was not measured it is difficult to pin down possible causes for this discrepancy, although it is likely that the numerical experiments delivered too little energy for the stronger specimens.

To avoid this kind of difficulty, Skempton [6] made a systematic effort to compare field and laboratory tests using only normalized blowcount. He found that the shape of the Meyerhof [51] expression was also valid when the normalized blowcount was employed, thus giving

$$\frac{N_{60}}{D_r^2} = B + C\frac{P_0}{100} \qquad (14)$$

Where B and C are material dependent parameters. Skempton [6] presented results indicating that, for normally consolidated sands, parameter B ranged between 17 and 46 and parameter C between 17-28.

Figure 13 presents the influence of overburden and relative density on the N_{60} values obtained from the simulations. The lineal influence of overburden and the quadratic influence of relative density are apparent in these results. When all the data is summarized in a single regression (Figure 14) it is observed that while the slope (C ~ 27) is very much in line with Skempton [6] values, the intercept value (B = 5) appears comparatively small. It should be noticed, however, that the field values quoted by Skempton [6] did carry significant uncertainty, as they were frequently obtained using reasonable guesses about the intervening variables (energy applied, efficiency, relative density or stress level). Figure 14 also includes the results obtained using downhole frozen samples by Hatanaka and Uchida [52]. It is noticeable how these experimental results also cluster in the low intercept range.

4. DYNAMIC VS STATIC RESISTANCE

It is interesting to compare the tip resistance obtained from the dynamic probes with the values that are obtained if the static penetration is continued to the same depths (Figure 15). Because of the large oscillations visible in the traces the comparison is best based on some representative statistics. The dynamic tip resistance q_d is thus obtained averaging the tip resistance measured during the "*deceleration*" phase (phase *II* in Figure 7). The reference static tip resistance q_e is obtained averaging the static tip resistance within the same depths. As illustrated in Figure 16a the mean values of dynamic and static tip resistances are very close to one another when they are below 10 MPa. Above this value the dynamic tip resistance is smaller than the static one. The 10 MPa limit also corresponds to a significant increase in the

magnitude of dynamic oscillations of tip resistance, as indicated by the standard deviations plotted in Figure 16b.

When cone penetration is performed at constant velocity there is a marked increase in tip resistance when the push velocity increases above 1 m/s [27, 28]. This increase is due to inertial effects kicking in above that limit. The peak velocity in the dynamic probes performed here is always above that limit, but reduces as penetration resistance increases (Figure 17). Note also that the time fraction spent above this inertial velocity limit is relatively small, due to the fast deceleration occurring in phase II (Figure 6). It is therefore unclear how inertial effects, by themselves, may explain the observed discrepancy between static and dynamic penetration values.

Other factors that seem relevant for this issue are energy limits, blowrate and contact model effects. Figure 18 illustrates the effect of density on the dynamic penetration curves at the highest confinement. It is evident that the plastic penetration at constant tip resistance that is characteristic of *phase II* is much reduced as density increases. It may be then inferred that in the denser more confined specimens the energy of the blow delivered was not enough to fully mobilized the available penetration resistance. Interestingly some of the tests in which the ratio q_d/q_e is smaller have blowcounts above or very close to the normalized limit for field test acceptance (N = 100).

Blow-rate may be also involved. Schnaid et al [53] showed that, after properly accounting for the energy input in the dynamic test, the tip resistance in static and standard penetration tests had very similar values, a result independent of the resistance value. Schnaid et al [53] performed SPT according to the standard procedure, delivering blow after blow until 30 cm of penetration was achieved. On the other hand, the simulations presented here included a single blow. For fast blow-rates there may be an overlap in the mechanical effects of separate blows. Unfortunately blow-rate is neither prescribed in standard procedures nor typically recorded.

Finally, it should be noted that the contact model employed here has some limitations to represent load-unload cycles. A somewhat excessive elastic compliance is included to alleviate a simplified description of contact mechanics in which, for instance, roughness-induced effects [54] are not considered. The increased contact density of denser specimens would make this limitation more relevant, as can be seen in the continuation of rebound after unloading in the curves of Figure 18. Ongoing work is exploring how to alleviate this problem using more refined contact models, in which the effect of contact roughness is included [55].

5. CONCLUSIONS

This work set out to explore the capabilities of the DEM VCC approach to model SPT. In this respect, and despite the limitations noted for the higher density specimens, the main results obtained appear very positive. These are

- The macro-element approach may be applied to model a driving rod with a realistic driving force input.
- Input energy normalization has been shown to be as effective an approach as in field testing.
- The effects of density and overburden pressure are in good agreement with well-established empirically –based expressions.

- In blows that result on fully developed plastic penetration, a close correspondence between dynamic and static tip resistance is observed.

Even if continuum based simulation models are advancing fast [56, 57] it is our impression that DEM VCC models do offer some advantages for the case of dynamic probing. The macro-element approach allows for easy generalization to represent more realistic impact dynamics, for instance by coupling it with driving tool models such as those presented by Daniel and Howie [58]. Consideration of drainage effects is also possible with resource to complementary modelling techniques, (e.g. CFD-DEM coupling, [59, 60]). But perhaps the most interesting applications will be those focusing on particle-scale influences on test result, such as grain crushing, gran size distribution effects or grain shape effects (either modelled directly or through a contact rolling resistance model). It is hoped that the work presented here will encourage those developments.

6. ACKNOWLEDGEMENT

The first author was supported by a CSC grant. This work was partly supported by the Ministry of Science and Innovation of Spain through the research grant BIA2017-84752-R and the EU H2020 RISE programme “Geo-ramp” (grant 645665).

7. REFERENCES

[1] Gourves, R., Barjot, R. (1995). “The Panda ultralight dynamic penetrometer”. *Proceeding of ECSMFE*. Copenhagen, Denmark, 83-88.

[2] Schnaid, F., Odebrecht, E., Rocha, M. M., Bernardes, G. De P., (2009). “Prediction of Soil Properties from the Concepts of Energy Transfer in Dynamic Penetration Tests.” *Journal of Geotechnical and Geoenvironmental Engineering* 135(May 2012): 1092–1100.

[3] Schmertmann, J. H., Palacios. A., (1979). “Energy Dynamics of SPT.” *Journal of the Geotechnical Engineering Division* 105(GT8): 909–926.

[4] Kovacs, W. D., Salomone, L. A. (1982). “SPT hammer energy measurement”. *Journal of Geotechnical and Geoenvironmental Engineering*, 108(GT4).

[5] Seed, H. Bolton, K. Tokimatsu, L. F. Harder, Riley M. Chung. (1985). “Influence of SPT Procedures in Soil Liquefaction Resistance Evaluations.” *Journal of Geotechnical Engineering* 111(12): 1425–1445.

[6] Skempton, A W. (1986). “Standard Penetration Test Procedures and the Effects in Sands of Overburden Pressure, Relative Density, Particle Size, Ageing and Overconsolidation.” *Géotechnique*, 36(3), 425–47.

[7] CEN ISO 22476-3 (2005). “Geotechnical investigation and testing -- Field testing -- Part 3: standard penetration test”

[8] ASTM D1586 -11. (2011). “Standard Test Method for Standard Penetration Test (SPT) and Split-Barrel Sampling of Soils.” In *Annual Book of ASTM Standards*, Philadelphia. papers2://publication/uuid/35B85424-852A-4B25-8883-63D2F4EF206B.

[9] Sy, A. Campanella, R. G., (1991) "An Alternative Method of Measuring SPT Energy". *International Conferences on Recent Advances in Geotechnical Earthquake Engineering and Soil Dynamics*. 2.

[10] Abou Matar, H., G. Goble. (1997). “SPT Dynamics Analysis and Measurements.” *Geotechnical and geoenvironmental engineering*, 123(10), 921–928.

[11] Odebrecht, E., Schnaid, F., Rocha, M. M., de Paula Bernardes, G. (2005). “Energy Efficiency for Standard Penetration Tests”. *Journal of Geotechnical and Geoenvironmental Engineering*, *131*(10), 1252–1263.

[12] DeJong, J. T., Ghafghazi, M., Sturm, A. P., Wilson, D. W., den Dulk, J., Armstrong, R. J., Davis, C. A. (2017). “Instrumented Becker Penetration Test. I: Equipment, Operation, and Performance”. *Journal of Geotechnical and Geoenvironmental Engineering*, 143(9), 04017062.

[13] Décourt, L., Quaresma Filho, A. R. (1994). « Practical applications of the standard penetration test complemented by torque measurements, SPT-T: Present stage and future trends”. In *Proceedings XIII ICSMFE*, New Delhi, Vol. 1, pp. 143-148. AA BALKEMA.

[14] Escobar, E. Benz, M. A., Gourvès, R., Breul, P. Chevalier, B. (2016) “In-situ determination of soil deformation modulus and the wave velocity parameters using the Panda 3®”; In *ISC5 Geotechnical and Geophysical Site Characterisation 5* – Lehane, Acosta-Martínez and Kelly (Eds) 279-284

[15] Gibbs, H. J., Holtz, W. G. (1957). “Research on Determining the Density of Sands by Spoon

Penetration Testing", *4th ICOSOMEF*, 1, 35-39

[16] Marcuson III, W. F., Bieganousky, W. A. (1977). "Laboratory standard penetration tests on fine sands". *Journal of Geotechnical Engineering Division*, *103*(GT-6), 565–588

[17] Ishikawa, K, Atsushi I., Ogura, H. and Shimohira, Y. (2013). "Estimation of Sand N -Value Using Pressurized Sand Tank and Verification of Vertical Loading Test of Model Pile." *AIJ J. Technol. Des* 19(41): 107–112

[18] Hatanaka, M., and Feng, L. 2006. Estimating density of sandy soils. Soils and Foundations J. 46(3): 299–314.

[19] Cundall, P A, and O. D. L. Strack. (1979). "A Discrete Numerical Model for Granular Assemblies." *Géotechnique* 29(1), 47–65

[20] Ahmed, S. M., Agaiby, S. W., and Abdel-Rahman, A. H. (2014). "A unified CPT–SPT correlation for non-crushable and crushable cohesionless soils". *Ain Shams Engineering Journal*, 5(1), 63-73

[21] Arroyo, M., Butlanska, J., Gens, A., Calvetti, F., Jamiolkowski, M. (2011). "Cone Penetration Tests in a Virtual Calibration Chamber." *Géotechnique*, 61(6): 525–531

[22] Zhang, Z., and Wang. Y., (2015). "Three-Dimensional DEM Simulations of Monotonic Jacking in Sand." *Granular Matter* 17(3), 359–376

[23] Ciantia, M. O., Arroyo, M., Butlanska, J., and Gens, A. (2016). "DEM modelling of cone penetration tests in a double-porosity crushable granular material". *Computers and Geotechnics*, 73, 109-127

[24] Holmen, J. K., Olovsson, L., and Børvik, T. (2017). "Discrete modeling of low-velocity penetration in sand". *Computers and Geotechnics*, 86, 21-32

[25] Butlanska, J., Arroyo, M., Amoroso, S., and Gens, A. (2018). "Marchetti Flat Dilatometer Tests in a Virtual Calibration Chamber," *Geotechnical Testing Journal*, 41(5), 930-945

[26] Escobar, E., Benz, M., Gourvès, R., and Breul, P. (2013). "Dynamic cone penetration tests in granular media: Determination of the tip's dynamic load-penetration curve". In *AIP Conference Proceedings* (Vol. 1542, No. 1, pp. 389-392). AIP

[27] Tran, Quoc Anh, Bastien Chevalier, and Pierre Breul. (2016). "Discrete Modeling of Penetration Tests in Constant Velocity and Impact Conditions." *Computers and Geotechnics*, 71, 12–18.

[28] Quezada JC, Breul P, Saussine G, Radjai F. (2014) "Penetration test in coarse granular material using Contact Dynamics Method". *Comput Geotech*, 55, 248–253.

[29] Zhang, N., and Evans, T. M. (2019). "Discrete numerical simulations of torpedo anchor installation in granular soils". *Computers and Geotechnics*, 108, 40-52

[30] Butlanska, J., Arroyo, M., Gens, A., and O'Sullivan, C. (2014). "Multi-Scale Analysis of Cone Penetration Test (CPT) in a Virtual Calibration Chamber." *Canadian Geotechnical Journal* 51(1), 51–66

[31] Plumelle, C., and Schlosser, F. (1991). "Three full-scale experiments of French project on soil nailing: CLOUTERRE". *Transp. Res. Rec*, (1330), 80-86

[32] Seif El Dine, B., Dupla, J. C., Frank, R., Canou, J., and Kazan, Y. (2010). "Mechanical characterization of matrix coarse-grained soils with a large-sized triaxial device". *Canadian*

Geotechnical Journal, 47(4), 425-438

[33] Jardine, R J, Z X Yang, P Foray, and BT Zhu. (2013). "Interpretation of Stress Measurements Made around Closed-Ended Displacement Piles in Sand." *Géotechnique* 63(8): 613–627

[34] Itasca Consulting Group. (2016). PFC3D: Itasca Consulting Group, Inc. (2014) PFC — Particle Flow Code, Ver. 5.0 Minneapolis: Itasca Consulting Group.

[35] Ting, J. M., Corkum, B. T., Kauffman, C. R., and Greco, C. (1989). "Discrete numerical model for soil mechanics". *Journal of Geotechnical Engineering*, 115(3), 379-398

[36] Calvetti, F., Di Prisco, C., and Nova, R. (2004). "Experimental and numerical analysis of soil–pipe interaction". *Journal of geotechnical and geoenvironmental engineering*, 130(12), 1292-1299

[37] Ciantia M. O., Boschi K., Shire T., and Emam S. (2018) "Numerical techniques for fast generation of large discrete-element models". Proceedings of the Institution of Civil Engineers - *Engineering and Computational Mechanics* 0 0:0, 1-15

[38] Zhang, N., Arroyo, M., Gens, A., and Ciantia, M. (2018a). DEM modelling of dynamic penetration in granular material. In *Numerical Methods in Geotechnical Engineering IX, Volume 1: Proceedings of the 9th European Conference on Numerical Methods in Geotechnical Engineering (NUMGE 2018)*, June 25-27, 2018, Porto, Portugal (p. 415). CRC Press.

[39] Zhang, N., Arroyo, M., Ciantia, M. and Gens. A., (2018b) DEM investigation of particle crushing effects on static and dynamic penetration tests. In *Proceedings of China-Europe Conference on Geotechnical Engineering (Wu W and Yu HS (eds))*. Springer, Cham, Switzerland, pp. 274–278

[40] Ciantia, M., Arroyo, M., Calvetti, F., and Gens, A. (2015). "An approach to enhance efficiency of DEM modelling of soils with crushable grains". *Géotechnique*, 65(2), 91-110

[41] Rorato, R., Arroyo, M., Gens, A., Andò, E., Viggiani, G., 2018. "Particle shape distribution effects on the triaxial response of sands : a DEM study", in: *Micro to MACRO Mathematical Modelling in Soil Mechanics*

[42] Ciantia, M. O., Arroyo, M., O'Sullivan, C., Gens, A., and Liu, T. (2018). "Grading evolution and critical state in a discrete numerical model of Fontainebleau sand". *Géotechnique*, 1-15

[43] Cundall, P. A. (1987). "Distinct element models of rock and soil structure". In *Analytical and computational methods in engineering rock mechanics* (ed. E. T. Brown), ch. 4, pp. 129–163. London, UK: Allen and Unwin

[44] Zhang, N (2019) Discrete element models of dynamic driving, PhD UPC (ongoing)

[45] Daniel, C. R., Howie, J. A., Jackson, R. S., and Walker, B. (2005). "Review of standard penetration test short rod corrections". *Journal of geotechnical and geoenvironmental engineering*, 131(4), 489-497

[46] Lee, C., Lee, J. S., An, S., and Lee, W. (2010). "Effect of secondary impacts on SPT rod energy and sampler penetration". *Journal of geotechnical and geoenvironmental engineering*, 136(3), 522-526

[47] Fairhurst, C. (1961). "Wave Mechanics of Percussive Drilling." *Mine and Quarry Engineering* 27(4): 169–78

[48] Schmertmann, J. H. (1979). "Statics of SPT." *Journal of the Geotechnical Engineering Division* 105(5): 655–670

[49] Idriss, I. M., and R.W. Boulanger. (2008). " Soil Liquefaction during Earthquakes".

[50] Schnaid, F., Odebrecht, E., Lobo, B. O., and Rocha, M. M. (2009b). Discussion of "SPT Hammer Energy Ratio versus Drop Height" by T. Leslie Youd, Hannah W. Bartholomew, and Jamison H. Steidl. *Journal of geotechnical and geoenvironmental engineering*, 135(11), 1777-1778

[51] Meyerhof, G. G. (1957). Disscussion on Research on determining the density of sands by spoon penetratio testing. Proc. 4th Int. Conf. Soil Mech. Fdn Engng, London 3, 110.

[52] Hatanaka, M., & Uchida, A. (1996). Empirical Correlation between Penetration Resistance and Internal Friction Angle of Sandy Soils. Soils and Foundations, 36(4), 1–9. https://doi.org/10.3208/sandf.36.4_1

[53] Schnaid, F., Lourenço, D., and Odebrecht, E. (2017). "Interpretation of static and dynamic penetration tests in coarse-grained soils". *Géotechnique Letters*, 7(2), 113-118

[54] Cavarretta, I., Coop, M., and O'Sullivan, C. (2010). "The influence of particle characteristics on the behaviour of coarse grained soils". *Geotechnique*, 60(6), 413-423

[55] Otsubo, M., O'Sullivan, C., Hanley, K. J., and Sim. W. W., (2017), "The influence of particle surface roughness on elastic stiffness and dynamic response." *Geotechnique* 67(5), 452-459

[56] Monforte, L., Arroyo, M., Carbonell, J. M., and Gens, A. (2018). "Coupled effective stress analysis of insertion problems in geotechnics with the Particle Finite Element Method". *Computers and Geotechnics*, 101, 114-129

[57] Moug, D.M., Boulanger, R.M., DeJong, J.T. and Jaeger, R.A. (2019), "Axisymmetric Simulations of Cone Penetration in Saturated Clay", *Journal of Geotechnical and Geoenvironmental Engineering*, 145 (4)

[58] Daniel, C. R., and Howie, J. A. (2005). "Effect of hammer shape on energy transfer measurement in the Standard Penetration Test". *Soils and Foundations*, *45*(5), 121–126

[59] El Shamy, U., and Aydin, F. (2008). "Multiscale modeling of flood-induced piping in river levees". *Journal of Geotechnical and Geoenvironmental Engineering*, 134(9), 1385-1398

[60] Climent, N., Arroyo, M., O'Sullivan, C., and Gens, A. (2014). "Sand production simulation coupling DEM with CFD". *European Journal of Environmental and Civil Engineering*, 18(9), 983-1008. DOI: 10.1080/19648189.2014.920280

[61] Iwashita, K., & Oda, M. (1998). Rolling resistance at contacts in simulation of shear band development by DEM. Journal of engineering mechanics, 124(3), 285-292

[62] Hettiarachchi, H., & Brown, T. (2009). Use of SPT Blow Counts to Estimate Shear Strength Properties of Soils: Energy Balance Approach. Journal of Geotechnical and Geoenvironmental Engineering, 135(6), 830–834. https://doi.org/10.1061/(ASCE)GT.1943-5606.0000016

8. Tables

Table 1 Physical properties of Fontainebleau sand

Database	D_{50}: mm	e_{min}	e_{max}	ρ_s	$\rho_{d,min}$: kN/m^3	$\rho_{d,max}$: kN/m^3
Exp: Luong and Touati (1983)	0.17	0.54	0.94	2.69	13.6	17.1
Exp: Seif El Dine et al. (2010)	0.21	0.54	0.94	2.65	13.4	16.9
NE34 FS: Ciantia et al. (2018)	0.21	0.51	0.9	2.65	13.7	17.2

Note: D_{50}, mean grain size; e_{min}, minimum void ratio; e_{max}, maximum void ratio; ρ_s, specific gravity; $\rho_{d,min}$, minimum dry density; $\rho_{d,max}$, maximum dry density

Table 2 DEM contact model parameters

Material	G: GPa	μ	ν
F-Sand	9	0.28	0.2
Rod	77	0.3	0.52

Table 3 Geometrical characteristics of the virtual calibration chamber

Variable (unit)	Symbol	DEM
Chamber diameter (mm)	D_c	760
Rod outside diameter (mm)	d_c	50.8
Chamber height (mm)	H	500
Scaling factor	-	79
mean element size (mm)	D_{50}	16.6
Chamber/rod diameter ratio	D_c / d_c=R_d	15
Rod/particle ratio	d_c / D_{50}=n_p	3.06

Table 4 Some characteristics of previous calibration chamber studies of SPT

Researchers	Range of D_r /%	Range of P_0 / kPa	Range of N	Container size	Radial BC	D_{50}/ mm	Proposed equation
Gibbs and Holtz /, Meyerhof (1957)	15-105	0-276	2-73	D_c=90 cm H=120 cm	Steel wall	1.58	$N = 1.7 \times \left(\frac{D_r}{100}\right)^2 (0.145P_0 + 10)$
Marcuson and Bieganousky (1977)	35-75	69-552	6-26	D_c =122 cm H=183 cm	Steel/rubber wall	0.23	$N = -5.5 + 0.2\left(0.145P_0\right) + 0.0046\left(D_r\right)^2$
Yamada et al. (1992)	24-89	49-294	10-37	D_c =50 cm H=70 cm	Triaxial cell	0.2	$N = 3.0 \times \exp\left(0.023D_r\right) \times \left(\frac{P_0}{98.1}\right)^{(1-0.0035D_r)}$
Ishikawa et al. (2013)	68-96	150-600	10-21	D_c =58.4 cm H=70 cm	Steel wall	0.54	$N = \exp\left(2.21\ln D_r + 0.646\ln P_0 - 10.437\right)$

Table 5 Parameters describing the simulated driving system

ρ_r (kg/m^3)	E (GPa)	c (m/s)	m_h (kg)	h (m)	g (m/s^2)	a (m^2)	A_h (m^2)	r (-)	L (m)	l (m)	t_{max}(ms)	$Fmax$ (kN)
8,050	200	4,984	63.5	0.76	9.8	0.002	0.008	0.25	0.97	10	4	251

Table 6 Basic programme of DEM-based dynamic probing tests

Test ID	D_r: %	P_0: kPa	N. of particles
Very Dense_100	82.6	100	69,166
Very Dense_200	83.0	200	69,166
Very Dense_400	83.7	400	69,166
Dense_100	74.0	100	66,059
Dense_200	74.7	200	66,059
Dense_400	75.7	400	66,059
Medium_100	62.1	100	60,031
Medium_200	62.9	200	60,031
Medium_400	63.9	400	60,031
Loose_100	40.7	100	50,335
Loose_200	41.7	200	50,335
Loose_400	43.2	400	50,335

Table 7 Results of DEM-based dynamic probing tests

Test ID	v_{peak}: m/s	q_d: MPa	$\Delta\rho$: cm	N	E_{blow}: J	ER: %	N_{60}	N/D_r^2	N_{60}/D_r^2
Very Dense_100	1.37	9.45	0.67	44	196	41.5	31	66	45
Very Dense_200	1.26	15.76	0.36	83	199	42.1	58	123	84
Very Dense_400	1.31	21.64	0.24	123	200	43.0	87	184	124
Dense_100	1.42	5.39	1.45	21	203	42.9	15	36	24
Dense_200	1.35	10.19	0.7	42	197	41.7	30	82	53
Dense_400	1.30	14.62	0.31	97	179	38.1	61	186	107
Medium_100	1.42	4.56	2.27	13	213	45.1	10	36	25
Medium_200	1.35	9.71	1.01	30	190	40.4	20	82	50
Medium_400	1.38	10.33	0.5	60	189	40.0	40	166	98
Loose_100	1.47	1.56	5.63	5	270	57.1	5	35	30
Loose_200	1.40	3.09	2.54	12	221	46.7	9	77	53
Loose_400	1.35	7.72	0.93	32	196	41.5	22	212	119

Table 8 Results from tests performed in similar conditions at different input energy

Test ID	η_d	F_{max} : kN	t_{max} : ms	$\Delta\rho$: *cm*	*N*	E_{blow}: J	*ER: %*	N_{60}	*ER*N*
Dense_100_0.7	0.7	175.7	4	0.66	45	105	22.0	17	9.9
Dense_100_0.9	0.9	225.9	4	1.14	26	163	34.5	15	9.1
Dense_100	1.0	251	4	1.45	21	203	42.9	15	9.03
Dense_100_1.2	1.2	301.2	4	2.05	15	292	61.9	15	9.3

9. Figures

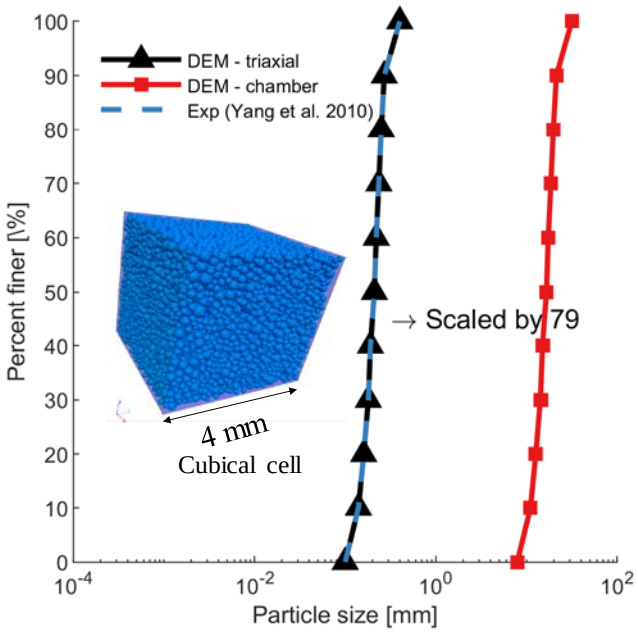

Figure 1 Particle size distribution of Fontainebleau sand and DEM models

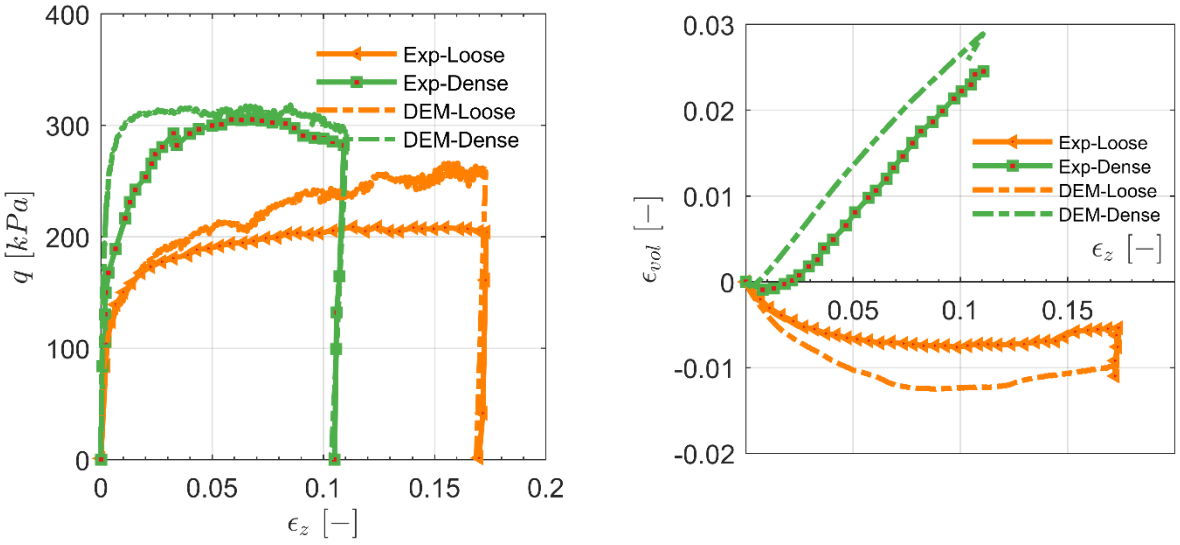

a) b)

Figure 2 Contact model calibration (G, μ, ν) with triaxial tests on Fontainebleau sand from Seif El Dine et al. (2010): a) q vs ε_z, b) ε_{vol} vs ε_z. Loose means at 30% relative density; dense at 70%

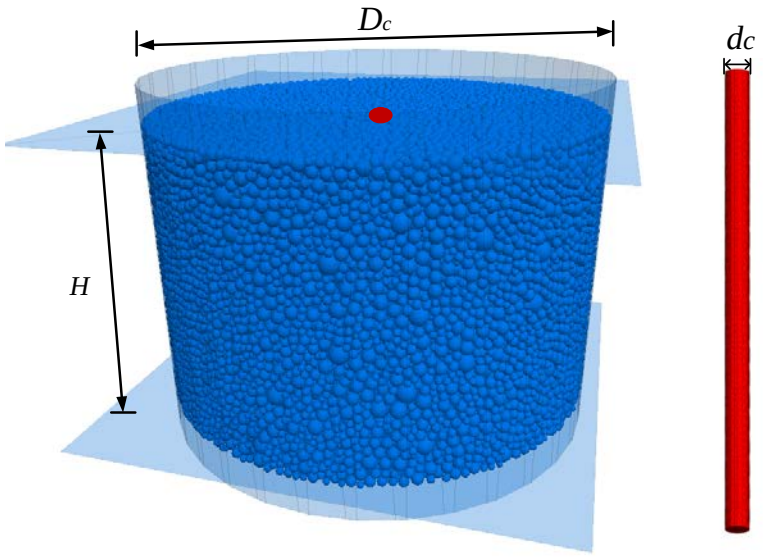

Figure 3 View of DEM model of calibration chamber and rod (flat-ended rod)

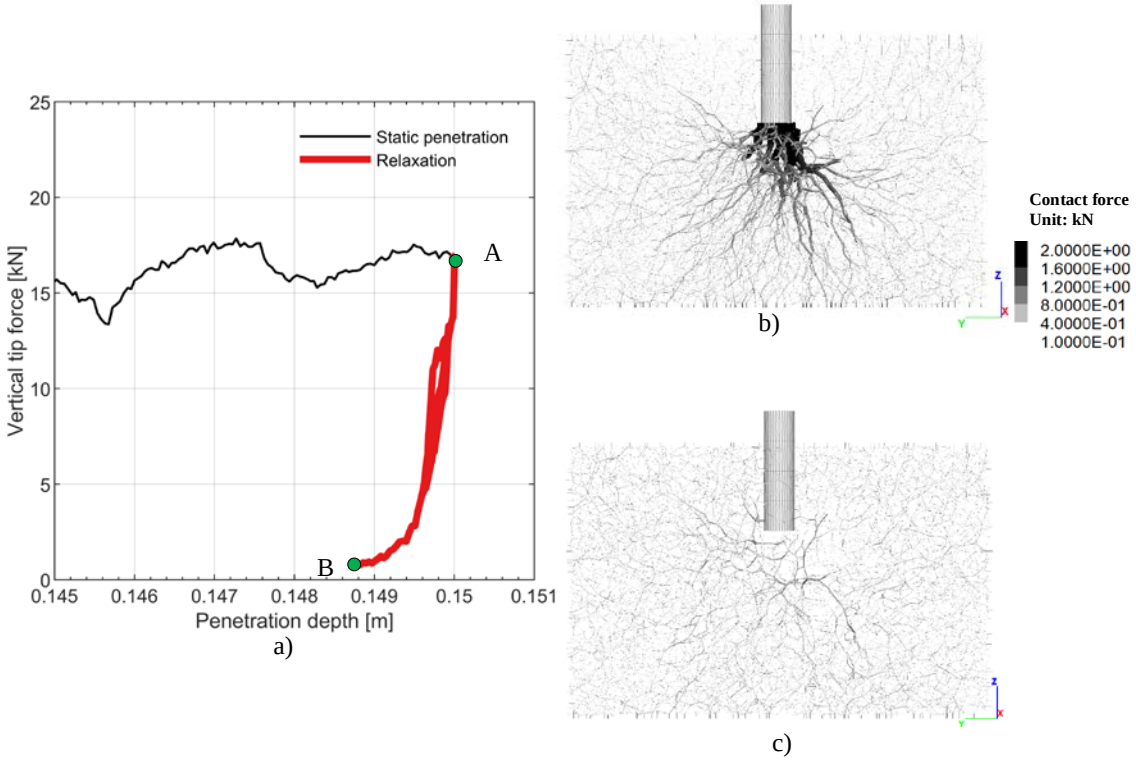

Figure 4. Residual force relaxation procedure (example: Loose_400): a) reduction of rod-particle contact force; b) contact force network at point A; c) contact force network at point B

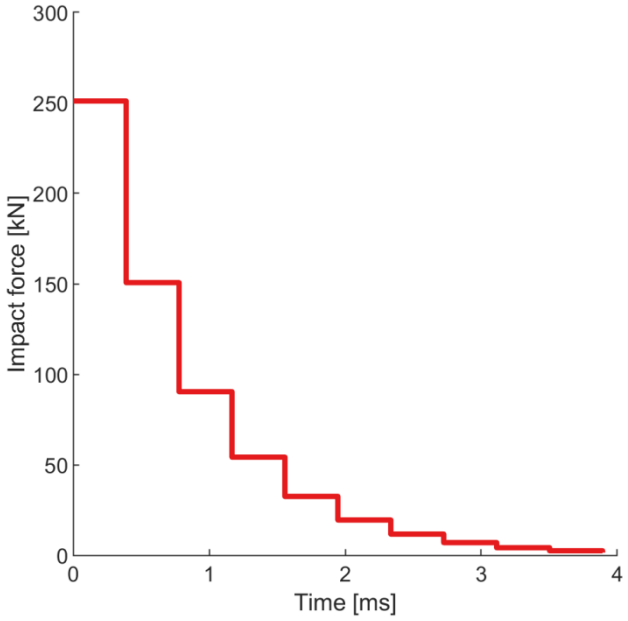

Figure 5 Base case for input driving force F_{drv}

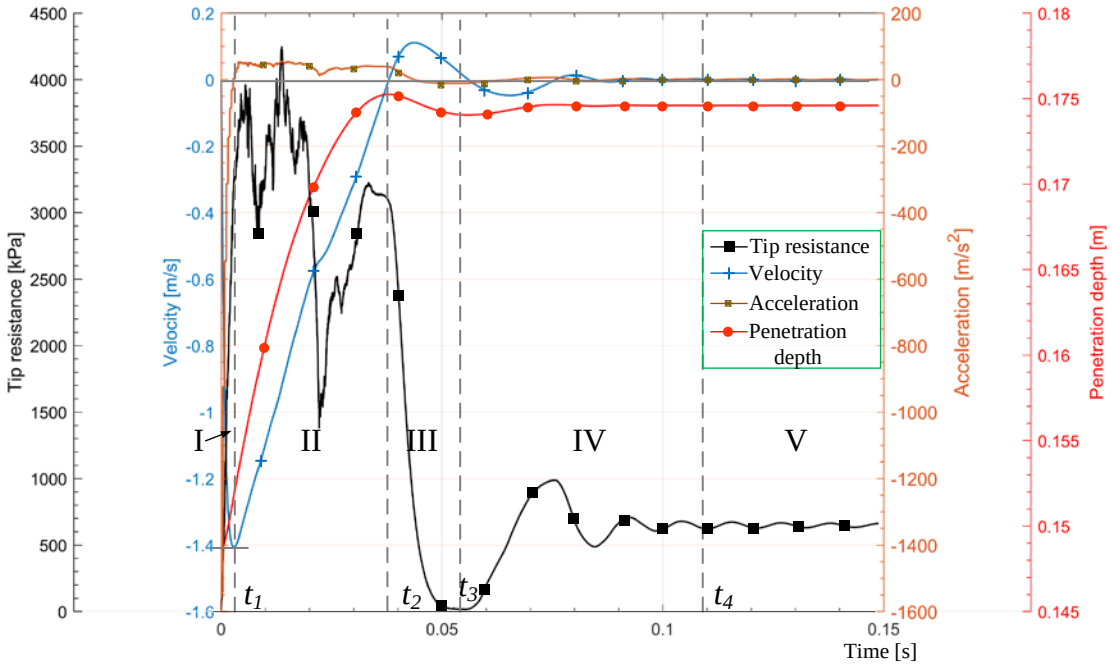

(a)

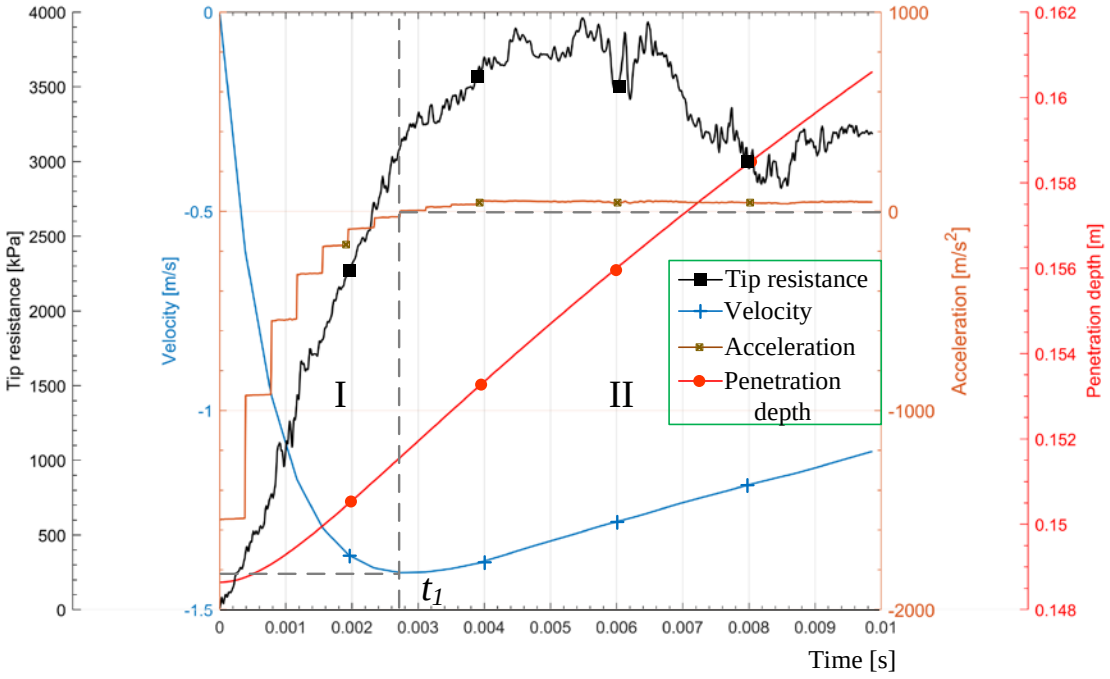

(b)

Figure 6 Evolution of tip resistance, rod velocity, rod acceleration and penetration depth during one impact with time in Test Loose_200: (a) full analysis; (b) zoom-in view till 0.01s

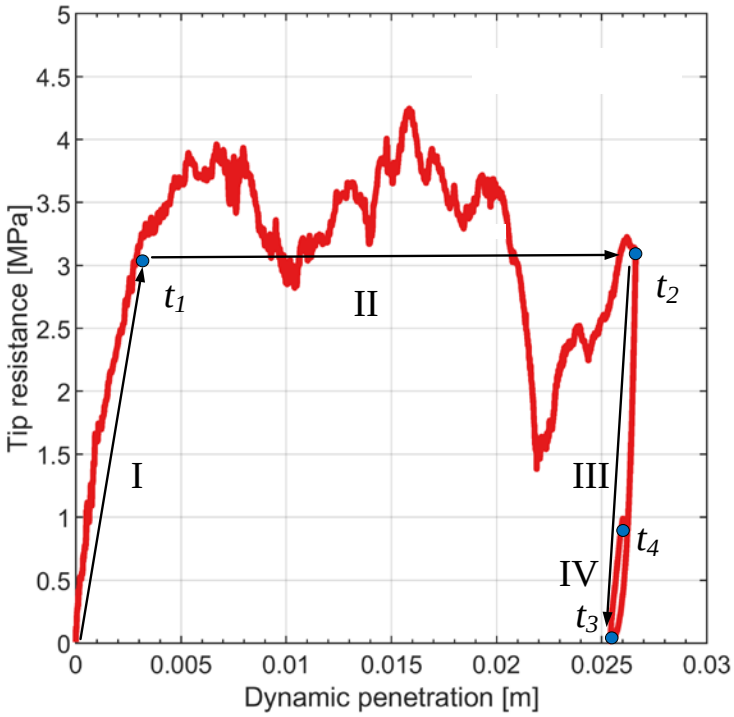

Figure 7 Example penetration curve during a blow (Loose_200, Table 6)

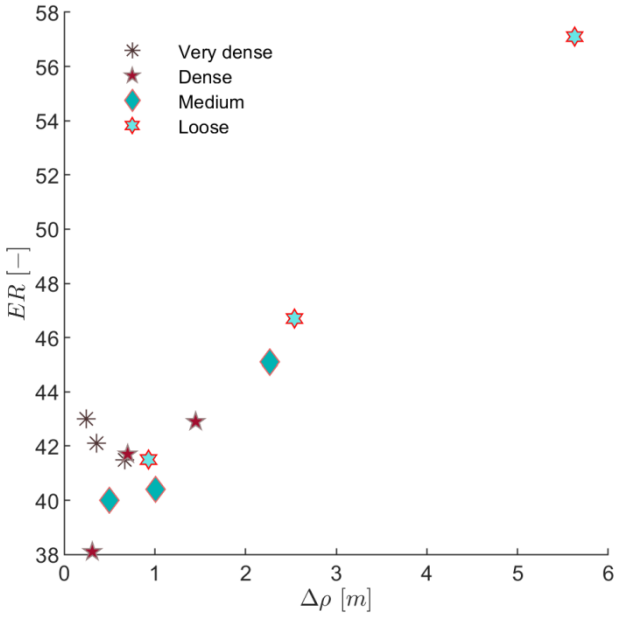

Figure 8 Energy input variations with blow depth

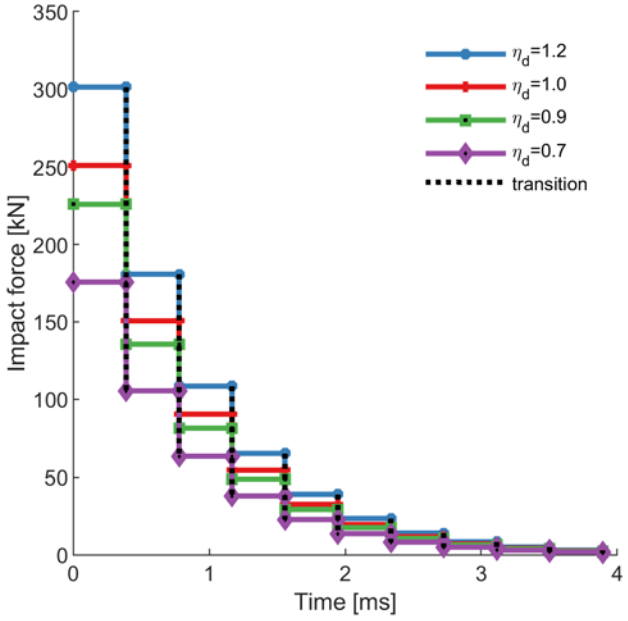

Figure 9 Various force-time input configurations

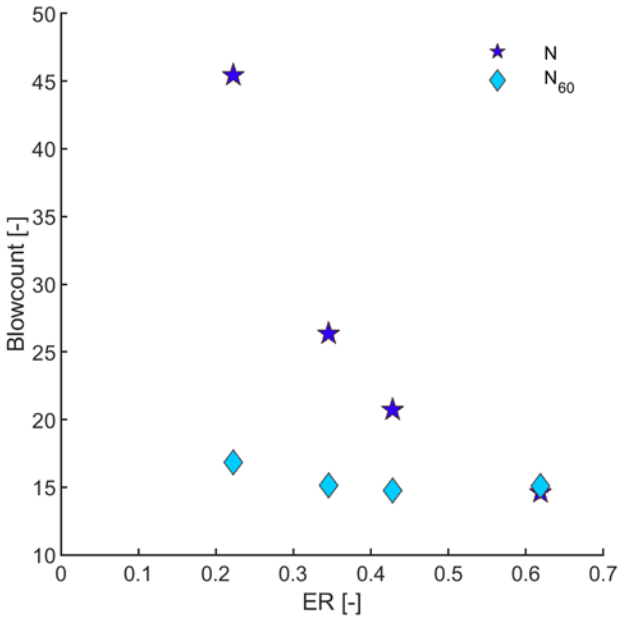

Figure 10 Raw and normalized blow counts versus energy ratio observed in one single blow

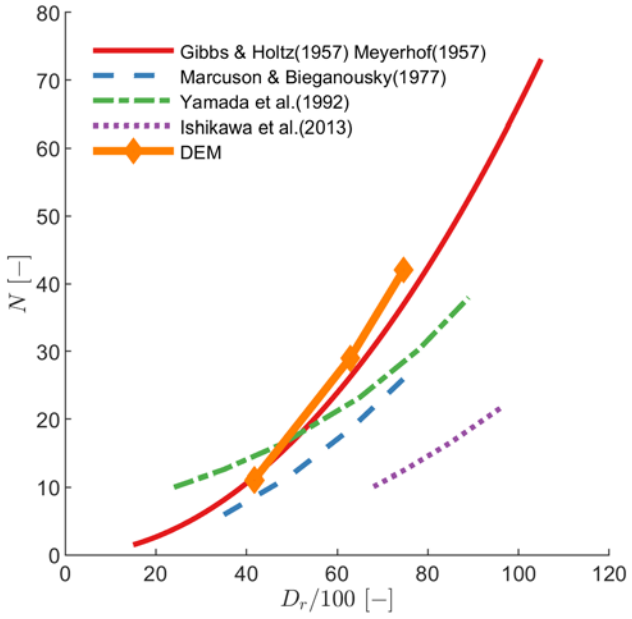

Figure 11 Relationship between Dr and penetration resistance at P_0= 200 kPa

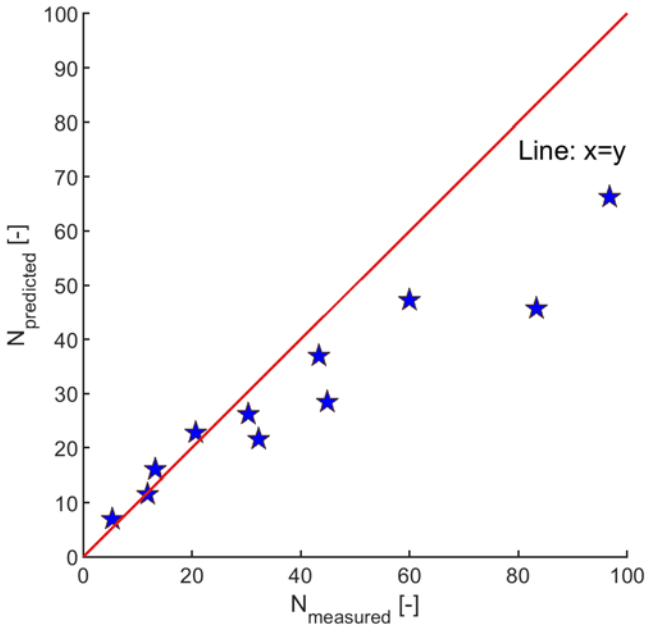

Figure 12 Measured blow numbers in SPT DEM simulation compared with those predicted by the Meyerhof expression (1957)

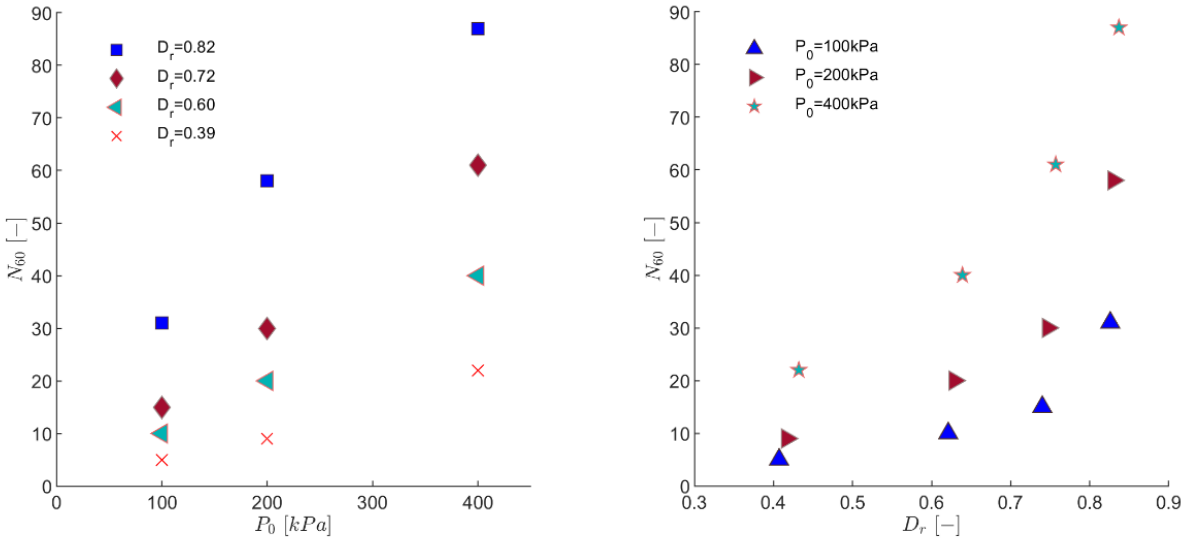

(a) (b)

Figure 13 Influence of (a) overburden (b) relative density on the normalized blowcount estimated from the simulations

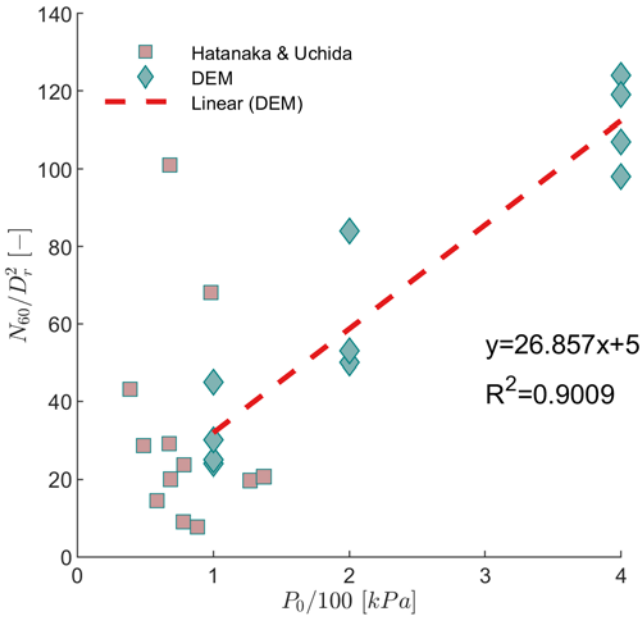

Figure 14 Comparison between normalized DEM results and test on frozen samples

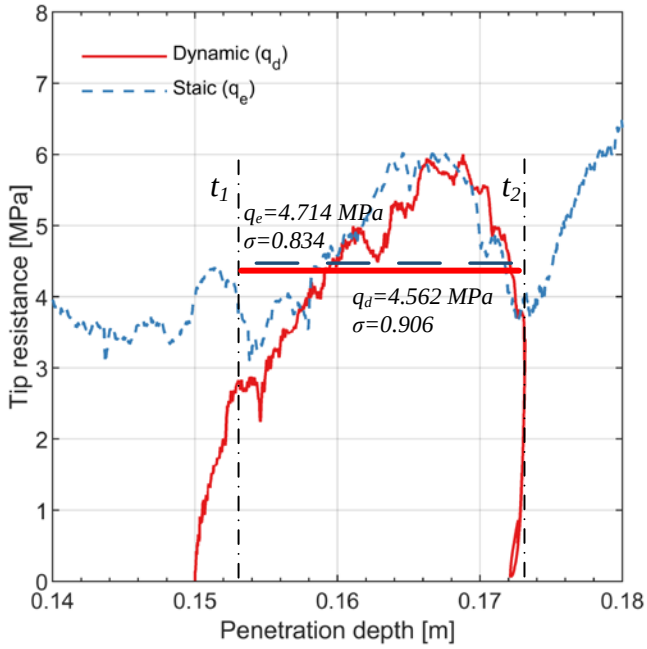

Figure 15 Example comparison of static and dynamic penetration (Medium_100)

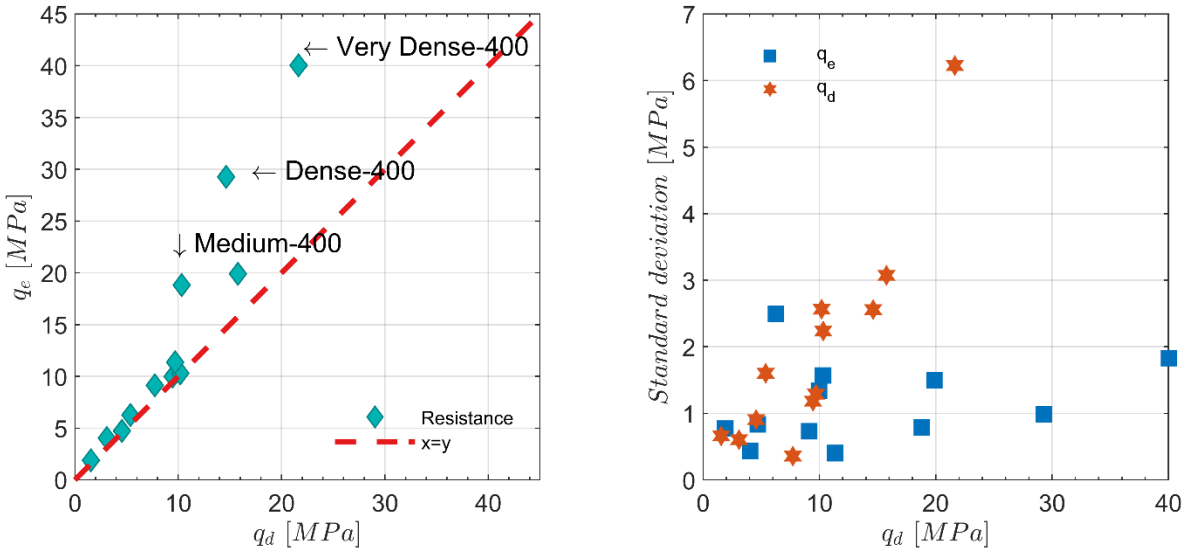

(a) (b)

Figure 16 q_e vs q_d and standard deviation of each case

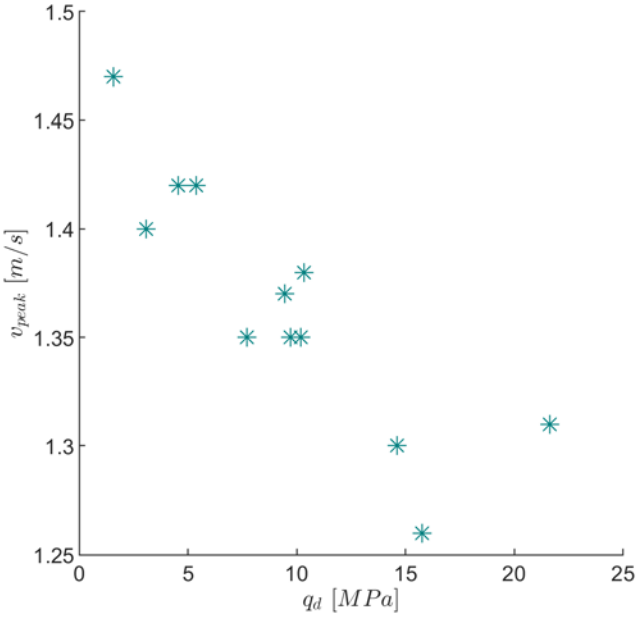

Figure 17 Peak velocity during dynamic probing vs average dynamic tip resistance

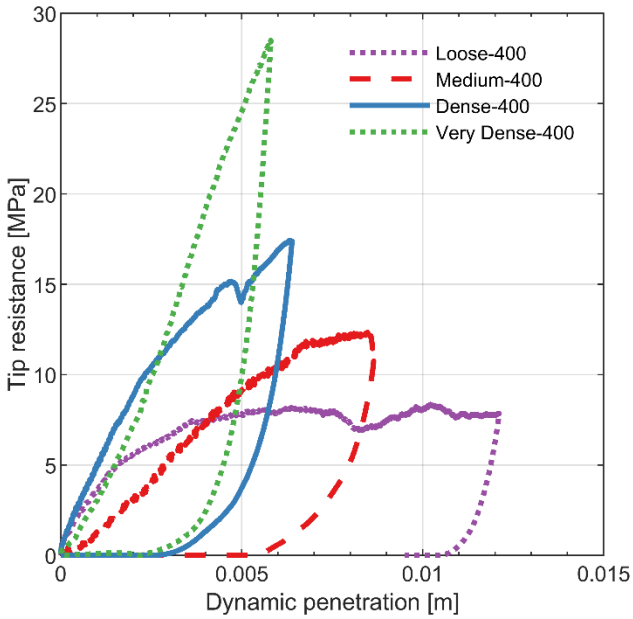

Figure 18 Influence of initial density on dynamic penetration curves for the series at P_0 = 400 kPa